Integrated Magnetic Nanoinductors

Aaron Seilis, *Student Member, IEEE*, Hamid Moghadas, *Member, IEEE*, Kambiz Moez, *Senior Member, IEEE*, and Mojgan Daneshmand, *Senior Member, IEEE*

***Abstract*— This paper demonstrates the feasibility of the realization of on-chip inductors for use in microwave and millimeter-wave devices using ultraminiaturized on-chip vertical nanohelices. The inductors are constructed by depositing a thin film of closely packed, vertically aligned Nickel nanohelices. The film is fabricated using a CMOS-compatible glancing angle physical vapor deposition method. The resulting nanostructured inductors are characterized from 10 to 70 GHz and are found to have inductances of 6 pH/μm^2, 60 times larger than conventional on-chip planar spiral inductors. A quality factor of three is measured and the results indicate that it continues to improve above 70 GHz, while inductance values remain relatively constant. The proposed nanostructured inductors can significantly reduce the chip area, and consequently the cost, of radio frequency and millimeter-wave integrated circuits. In addition, the nanostructured inductors offer significantly larger operation bandwidth than on-chip planar structures operating at frequencies above 100 GHz.**

***Index Terms*— Glancing angle deposition, inductors, magnetic materials, millimeter-wave measurements.**

I. Introduction

THANKS to the continuous advance in semiconductor fabrication processes, particularly CMOS technology, transistor dimensions have been continually scaling down to increase the density of circuits, decrease power consumption, and increase system functionalities over the last few decades. However, the dimensions of on-chip passive components, especially inductors, have shrunk at much slower rate than the minimum feature size of commercial semiconductor processes. As a result, the continuous need for large on-chip inductors and other bulky passive components has made the realization of radio frequency (RF) and millimeter-wave integrated circuits of equal density to their digital counterparts impossible. Therefore, there is a growing need for alternative implementations of on-chip inductors.

For discrete devices, solenoid and toroid structures are known to produce high-density inductances; however, these structures are 3-D and require many process steps to implement on-chip [1]. The performance of 2-D configurations (e.g., planar spiral inductors) depends on substrate parameters. These configurations exhibit low inductance and require a large amount of area in comparison with other circuit components [2]. Modern 2-D (multilayer) inductor structures have inductance densities lower than 0.1 pH $\cdot$ μm^{-2} implemented in areas from 10^4 μm^2 to 5 mm^2 [3], [4], [8]–[14].

At millimeter-wave frequencies, substrate losses reduce self-resonance frequencies of planar coils. Above 30 GHz, vertically stacked planar inductors have been shown to reduce the on-chip area [3] at the cost of increasing the number of metal layers and consequently a more complicated fabrication process [4]. Other methods to reduce substrate losses are to use Microelectromechanical System fabrication techniques to build planar inductors which are rotated into a vertical position by thermal stress or magnetic actuation [5]. Vertically rotated inductors have better electrical performance characteristics than their horizontal counterparts. However, Zou *et al.* [5] still require the same on-chip area during fabrication and may introduce additional packaging issues related to placing large vertical structures on a substrate.

Several efforts to use nanostructured films to realize inductors have been reported, however, these devices are challenging to build reliably. One common technique uses carbon nanotubes as inductors [6]. While carbon inductors can theoretically produce very high inductance, the circuit integration and the high contact resistance remains challenging [7]. Alternatively, stress-induced coiled film inductors produce a very high inductance, but are narrowband with a self-resonance of about 300 MHz [1]. Besides, the stress-formed helix and multiwall carbon nanotube both require manual fabrication techniques that are not easily scalable to production-scale reliabilities.

This paper demonstrates that magnetic vertically aligned nanowire array films can be used as area efficient inductors with an inductance density of 6 pH/μm^2 which makes it a perfect candidate for on-chip integrated circuits. This ultra-broadband device has constant inductance in Ku, Ka, V, and W bands and its self-resonance frequency in terahertz range is much higher than traditional planar loop and spiral structures [3], [4], [8]–[18]. Furthermore, it is fabricated with a reliable glancing angle physical vapor deposition (GLAD) process that is repeatable, CMOS compatible, and simpler than the process used for fabrication of other nanoinductors [19]. The fabrication process of this nanoinductor film is detailed in Section II. Section III explains the film principle of operation. The measurement technique, the discussion on quality factor, and power handling analysis are

Manuscript received September 8, 2014; revised December 22, 2014 and February 17, 2015; accepted April 12, 2015. Date of publication May 6, 2015; date of current version May 27, 2015. This work was supported in part by CMC Microsystems, in part by the Natural Sciences and Engineering Research Council of Canada, in part by the Alberta Innovates-Technology Futures, and in part by Micralyne, Inc., Edmonton, AB, Canada. Recommended for publication by Associate Editor D. G. Kam upon evaluation of reviewers' comments.

A. Seilis is with Ciena Corporation, Ottawa, ON K2H 8E9, Canada (e-mail: aaron.seilis@ualberta.ca).

H. Moghadas, K. Moez, and M. Daneshmand are with the Department of Electrical and Computer Engineering, University of Alberta, Edmonton, AB T6G 2V4, Canada (e-mail: hmoghada@ualberta.ca; kambiz@ece.ualberta.ca; mojgan@ece.ualberta.ca).

Color versions of one or more of the figures in this paper are available online at http://ieeexplore.ieee.org.

Digital Object Identifier 10.1109/TCPMT.2015.2426111

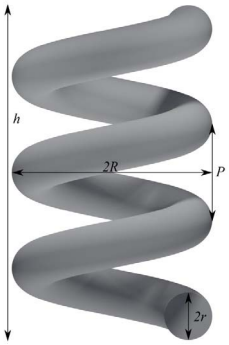

Fig. 1. Physical parameters for a helix. R is the major radius of the helix, r is the minor radius of the helix (the wire radius), P is the pitch of the helix, and h is the total height ($h = NP$, where N is the number of turns in the helix).

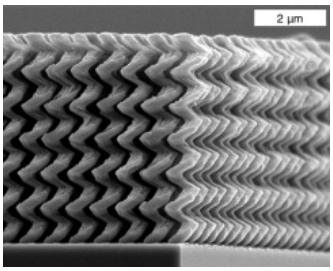

Fig. 2. SEM image of a regular helix array created using the GLAD technique.

elaborated in Section IV. Finally, the conclusion is given in Section V [20].

II. Fabrication of Vertically Aligned Magnetic Nanoinductors

The proposed inductor films can be deposited by the *glancing angle deposition* technique. GLAD-deposited films have nanoscale features which can be controlled though substrate rotation and deposition angle [19]. The types of structures possible through GLAD include posts and helices, useful for inductor applications. Fig. 1 shows a helix array that was deposited using the GLAD technique, demonstrating the high level of control that is achievable over the film structure. The individual structures in the film have nanometer-scale cross sections, which makes them suitable for low-area inductive elements. GLAD films are fabricated using reliable physical vapor deposition (PVD) processes [21]. GLAD structures require collimated vapor flux, highly oblique deposition angles, and low substrate temperatures (allowing compatibility with existing CMOS technologies). The combination of collimated vapor flux and atomic scale roughness allows a self organizing accumulation of material at column tips. The vapor flux's orientation can be controlled during deposition, allowing the helical structures to be tailored for application-specific design criteria. The parameters of a helix are shown in Fig. 1; these can be controlled via the deposition angle, deposition rate, and deposition time. A regular array, such as the one shown in Fig. 2 can be created by seeding the helix locations prior to the deposition process. For the devices studied here, no substrate seeds were used.

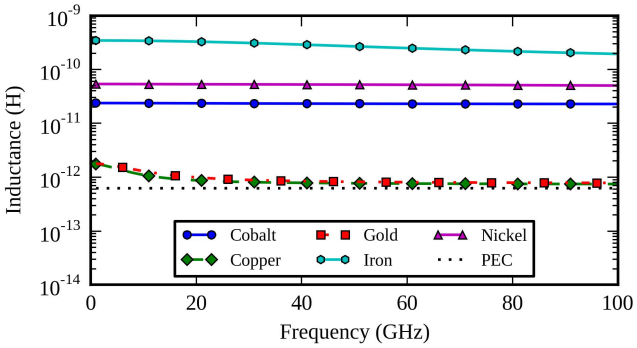

Fig. 3. Inductance of a single helix in free space for different coil materials.

Our devices were produced using e-beam deposition in a custom high vacuum chamber (Kurt J. Lesker, AXXIS). The base pressure was below 50 μPa for all depositions. The source material was 6–12-mm nickel (Ni) spheres (99.9% purity, Cerac, Inc.) located 42 cm from the substrates. To facilitate electrical connection with the Ni film, coplanar interdigital electrode (IDE) structures were used as the substrate [22]. Prior to deposition, two pieces of kapton tape were placed on the substrate perpendicular to the IDE electrodes to isolate the devices. The vapor flux incidence angle was 81° and the deposition rate was 0.65 nm s^{-1} (measured by crystal thickness monitor). This results in helix parameters of: $R = 82.15$ nm, $r = 35.71$ nm, $P = 457$ nm, and $h = 500$ nm. The ease of the GLAD process is a distinct advantage over other nanotechnology-based devices for inductors, which often require electron-beam lithography [7], atomic force microscopy [23], or other methods unsuitable for mass manufacturing [1].

The most important limitation of GLAD film is the simulation of the devices incorporating it due to the extremely high aspect ratio of the model. The high aspect ratio is caused by the nanosize of GLAD wires and the millimeter size of electronic ports which are used for utilizing GLAD.

III. Principles of Operation

We propose using highly packed magnetic vertical nanowires, similar to Fig. 2, to develop area efficient inductors. The characteristics that distinguish this type of structure from traditional materials are anisotropic conductivity and high permeability of the inductor wire and the surrounding medium. These properties allow for the construction of new inductive devices with improved inductance density.

A. Helix Wire Material

The helix nanowire material has a strong effect on the performance of the inductor, especially in the case of magnetic materials [24]. This is due to the fact that small cross sections, such as those of nanowires, are smaller than the skin depth; therefore, the current penetrates through the entire single nanowire cross section.

Fig. 3 shows the inductance of a single nanohelix simulated by Ansys High Frequency Structure Simulator (HFSS) for

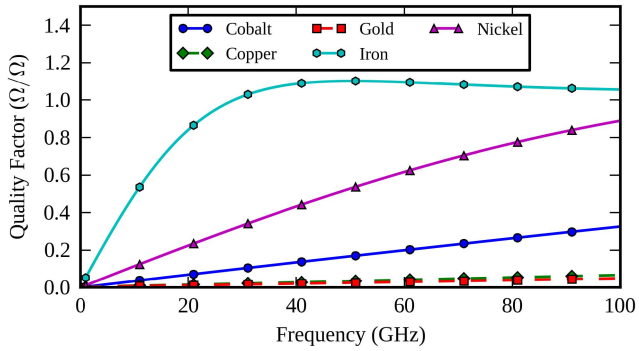

Fig. 4. Quality factor of a single helix in free space for different coil materials.

several materials (using the parameters summarized in Section II). The nonmagnetic materials all exhibit small inductances, on the order of 10^{-12} H; however, the magnetic elemental metals (colbalt, $\mu_r = 250$; nickel, $\mu_r = 600$; and iron, $\mu_r = 4000$) have inductances that are over an order of magnitude higher than the nonmagnetic metals. This increase in inductance is due to the interaction of the magnetic field with the magnetic wire material. Fig. 3 shows that at millimeter-wave frequencies, the resulting inductance is shown to be approximately proportional to the relative permeability of the material.

While iron produced the best inductive performance in simulation, GLAD iron films are complex due to material kinetic effects [26]. We therefore chose Ni helices in this paper.

The quality factor was calculated by (1) using the Z-parameters output by HFSS. Corresponding to the increase in inductance, the quality factors of the magnetic materials are also increased, as shown in Fig. 4. The quality factors increase at millimeter-wave frequencies because of the large improvement in inductance and only small change in resistance

$$Q = \frac{\text{Imag}(Z_{11})}{\text{Real}(Z_{11})} = \frac{\omega L}{R}. \tag{1}$$

B. Behavior of Nanowire Array

Since the film is entirely constructed from nanowires, the behavior of individual helices becomes a significant factor in the overall film's inductive performance. The simplest assumption about a helix array encapsulated between two ports is the parallel combination of resistors (R_{helix}) and inductors (L_{helix}) which is simply analyzed. However, due to the closely packed subwavelength structure of the array, there will be a very strong mutual coupling (M) between these inductors. Hence, the inductive performance of the single helix is improved by the high permeability and the magnetic mutual coupling with surrounding wires. There is also a capacitive coupling between adjacent wires which is negligible. Besides, there will be a parasitic capacitance ($C_{\text{parasitic}}$) between the top and bottom port caps used to electrically connect to the film. Based on these initial assumptions, the equivalent circuit network of the film is demonstrated in Fig. 5(a). The film behaves as a 2-D array of this network.

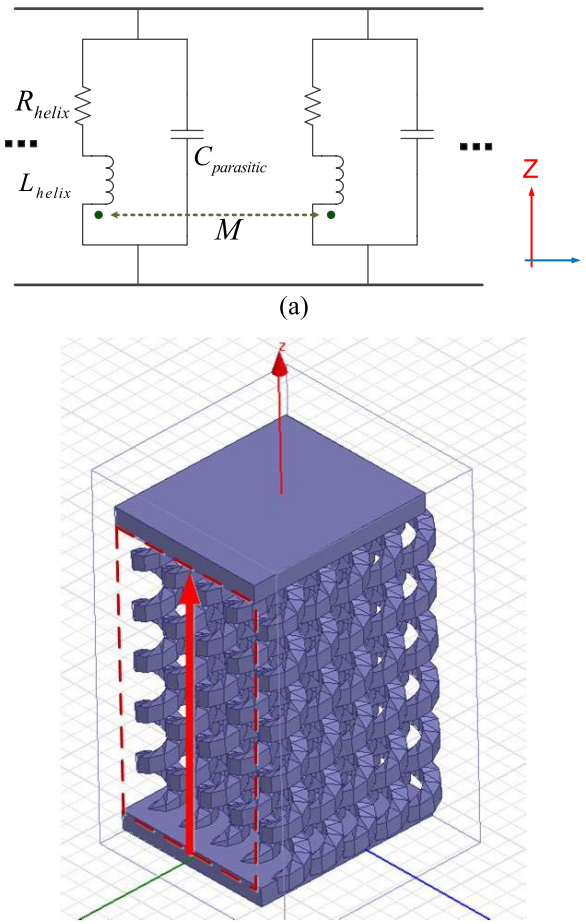

Fig. 5. (a) Equivalent circuit network of the GLAD film. (b) 5×5 array of helices in electromagnetic simulator. Pad size = 1 μm $\times$ 1 μm $\times$ 100 nm. Air box = 1.2 μm $\times$ 1.2 μm $\times$ 2 μm.

To inspect the array effect, several arrays with different $N \times N$ size are simulated and compared with the performance of a single helix. Fig. 5(b) shows the model of a 5×5 array. The model is excited by a waveport in ANSYS HFSS which touches both pads and the whole model is placed in a vacuum box with radiation boundary. Fig. 6(a) shows that the inductance is reduced as the array size grows. This result is also expected since the total inductance is reduced when ideal inductors are placed in parallel. Fig. 6(b) shows the quality factor of the helix array as the array size increases.

The inductor resonance frequency is inspected by the frequency behavior of Q. The wideband analysis of a 5×5 array is shown in Fig. 6(c). It is clear from the simulations that the nanoinductors potentially have resonance frequency in terahertz range which highlights it potentials in wideband applications.

The effect of array periodicity (d) is inspected in Table I for a 5×5 nanowire array at 10 and 100 GHz. As d decreases (denser array), L and Q rise due to increased M.

C. Effect of Surrounding Helices on a Single Helix

In a GLAD film, the helices form an array of closely packed nanowires, with subwavelength spacing. This fine structure

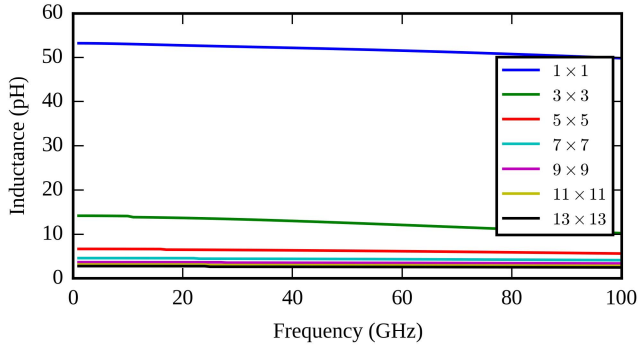

(a)

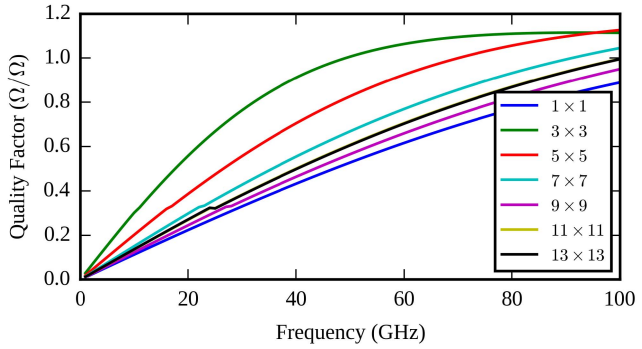

(b)

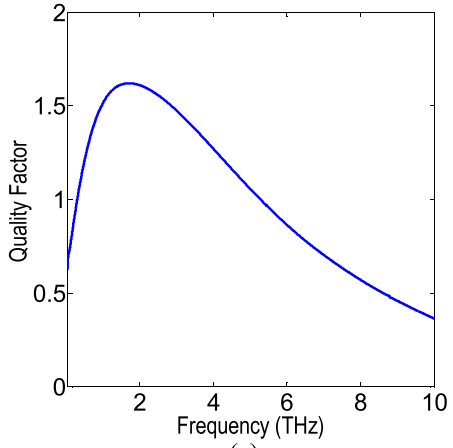

(c)

Fig. 6. Simulated Ni helix arrays (considering bulk Ni conductivity). (a) Inductance. (b) Q. (c) Wideband analysis of a 5×5 array of helices.

TABLE I
EFFECT OF WIRE PERIODICITY

	L(pH)		Q	
d (nm)	*10 GHz*	*100 GHz*	*10 GHz*	*100 GHz*
60	11.8	8.2	0.19	0.88
150	8.5	5.9	0.16	0.8
200	7.2	5.1	0.14	0.73

means that the material can be treated as an effective medium. Due to the vertical connection of the nanowires and horizontal gap between the wires, this effective medium is considered to

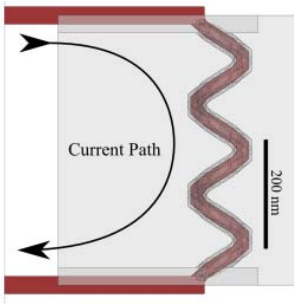

Fig. 7. Model of a single helix element (red) embedded in a uniform anisotropic film (gray area). The vertical line on the left side is the port plane.

have an anisotropic conductivity that is large in the vertical direction and small in the horizontal direction. Anisotropic conductivities can easily be described using a tensor, shown in (2), where σ_{xx} is the conductivity in the $\hat{x}$ direction, σ_{yy} is the conductivity in the $\hat{y}$ direction, and σ_{zz} is the conductivity in the $\hat{z}$ direction. For the case of vertically aligned nanowires, the film is only conductive in the vertical direction, making σ_{zz} the only nonzero element in the conductivity tensor. In addition to the anisotropic conductivity, the material has a large effective permeability inherited from the wires. A simple model for the helix embedded in a homogeneous material is shown in Fig. 7

$$\overleftrightarrow{\sigma} = \begin{pmatrix} \sigma_{xx} & 0 & 0 \\ 0 & \sigma_{yy} & 0 \\ 0 & 0 & \sigma_{zz} \end{pmatrix}. \tag{2}$$

The simulated structure has a port on the left side; the top conductor wire is stimulated by the wave port and the bottom wire is connected to ground. The current path is indicated by the black arrow.

It is well known that the use of ferromagnetic materials in inductor core structures can greatly increase a device's inductance. However, ferromagnetic devices are not widely used in integrated devices due to high eddy currents [26]. In this anisotropic structure, these eddy currents are significantly reduced due to the film's anisotropic conductivity, leading to higher inductance values than a bulk Ni film.

Due to the fact that the materials produced by thin film processes often differ from their bulk equivalents, the conductivity cannot be assumed to be equal to the bulk value. Ni bulk conductivity of 1.4×10^7 S/m decreases to 75 000 for nanohelices [27]. Therefore, assuming a relative permeability of $\mu_r = 600$ (the value of bulk Ni), the effect of a conductive surrounding material with different conductivity was simulated. Fig. 8(a) shows the inductance of the helix structure when surrounded by a conductive material. The inductance is highly dependent on the conductivity of the surrounding material. It clearly indicates that the inductance of a single helix is highest when the surrounding material is nonconductive or low conductive. It can be seen that as the conductivity is increased above $\sigma = 10^4$ S/m, the inductance is decreased. This effect is caused by the shielding of the conductive surrounding film that reduces the

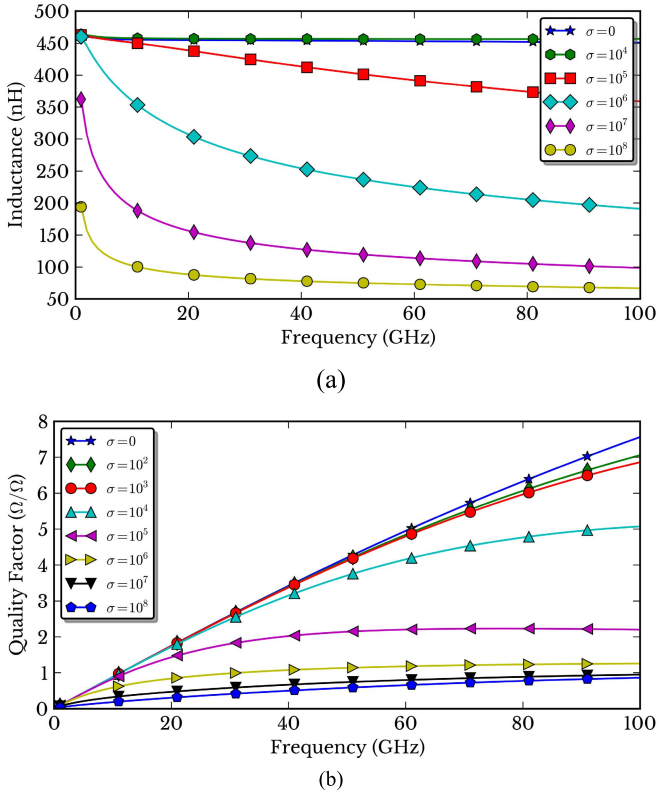

Fig. 8. Single helix embedded in a conductive magnetic medium ($\mu_r = 600$). (a) Inductance. (b) Quality factor.

penetration of the field produced by the helix and fades the surrounding medium effect. Also, Fig. 8(b) shows that the Q increases as the conductivity of surrounding medium decreases.

D. Simulation Model: A Homogeneous Film

Due to the large computational requirements of the helical model presented in the previous sections, and the packed nature of the GLAD Ni inductive film, a bulk effective-medium model of the nanostructured thin film was developed. The model, as shown in Fig. 9, utilizes an anisotropic material with a horizontal conductivity of 0 and a permeability equal to Ni ($\mu_r = 600$). The film is connected to the port by a large conductor on the top (the signal) and a set of smaller conductors on the bottom (the ground).

Fig. 10 shows the simulated inductance of the homogeneous film with a range of conductivities. The inductance decreases as conductivity is increased because of the reduced magnetic field penetration into the film due to the skin effect. The inductances in Fig. 10 follow a decreasing trend, similar to the isotropic Ni film in Fig. 8. This is because the top conductor allows for horizontal connections between locations in the film, which allows for eddy currents to form, causing the skin effect. However, the effect is reduced from an isotropic film. The film inductance is reduced from the single helix case, due to the increased width of the current path. This increased width is the equivalent of putting multiple inductors in parallel.

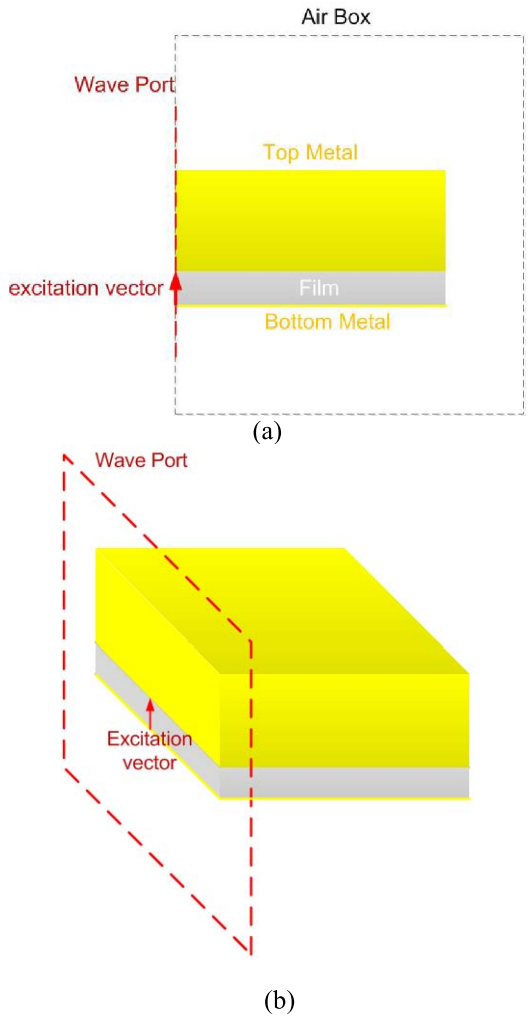

Fig. 9. Homogeneous film. (a) Side view of the simulation model. (b) 3-D view of the simulation model.

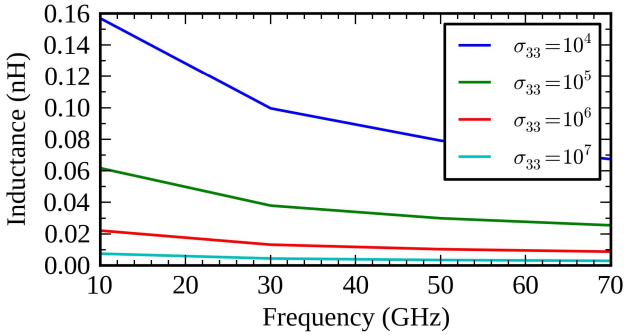

Fig. 10. Inductance of the homogeneous film model. For the higher conductivities, the inductance becomes flatter over the simulated bandwidth.

IV. Measurement

A. Inductance Measurement

To validate the above simulations, an anisotropic Ni film with a thickness of approximately 500 nm is fabricated on gold IDE and characterized [28]. To measure the film's inductance, the top of the film is connected using a conductive

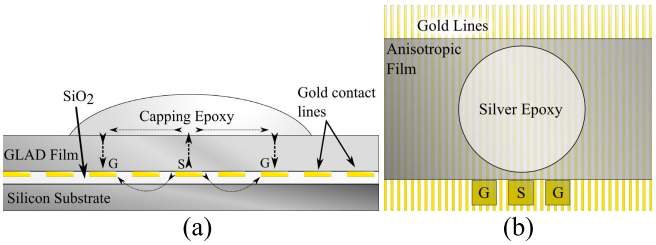

Fig. 11. (a) Cross section of the test structure. The dashed lines show the current paths and the G–S–G labels indicate the probe configuration. (b) Top-down view of the structure. The silver epoxy lies directly on top of the anisotropic film and does not contact the substrate or test lines. Note that each probe contact touches multiple gold lines.

silver epoxy. This capping layer connected the signal and ground terminals through the GLAD film. It is possible to grow a capping layer directly on the GLAD during the initial growth step [21]; however, this was not done for our samples to facilitate the lift-off and fabrication process. This also allowed for direct observance of the helices to assure the integrity of the inductors prior to capping. Instead, the silver epoxy was applied as a postprocess to form a capping layer and later extracted from the measured results. Characterization with a scanning electron microscope has verified that the silver flakes in the epoxy lie on top of the film with no penetration. The epoxy material itself is not conductive, thus the silver epoxy provides a good capping layer. Fig. 11(a) shows a schematic of the cross section of the test structure, including substrate layers and capping layer. The layout of the gold lines and the GLAD film on top is shown in Fig. 11(b). Cascade Microtech RF probe station is used for measurements (Fig. 12). The SEM image of fabricated GLAD is shown in Fig. 13. The gold lines and silver epoxy are beneath and above the film, respectively. The G–S–G label indicates the CPW probe touchdown location next to the film. Fig. 14(a) shows a false color SEM image of the fabricated film, gold lines, and silver epoxy capping layer. The film was grown on top of closely spaced gold lines (100-nm thickness) that were embedded in a 1-μm silicon dioxide layer, grown on a low resistivity silicon substrate. Fig. 14(b) is the top view of the fabricated prototype showing the silver flakes of epoxy. After fabrication, the S-parameters of the device were measured from 10 to 70 GHz.

To find the exact impedance of GLAD film, first, the whole measurement setup should be calibrated, and then the measurements should be analyzed and extracted. The G–S–G probes are calibrated using the software package installed on the system and the calibration standards which are suitable for the G–S–G probes, including matched load, open circuit, and short circuit, and through (SOLT). Fig. 12(c) shows the two microprobes on left and right which are connected to the open circuit standard. Before connecting the G–S–G probes to standard loads, the software requires us to measure the probes individually as they are kept in air at a sufficient height above substrate to account for probe parasitics in calibration calculations.

To find the film inductance value (Z_{GLAD}), this S-parameter measurement cannot be directly transformed to Z-parameters

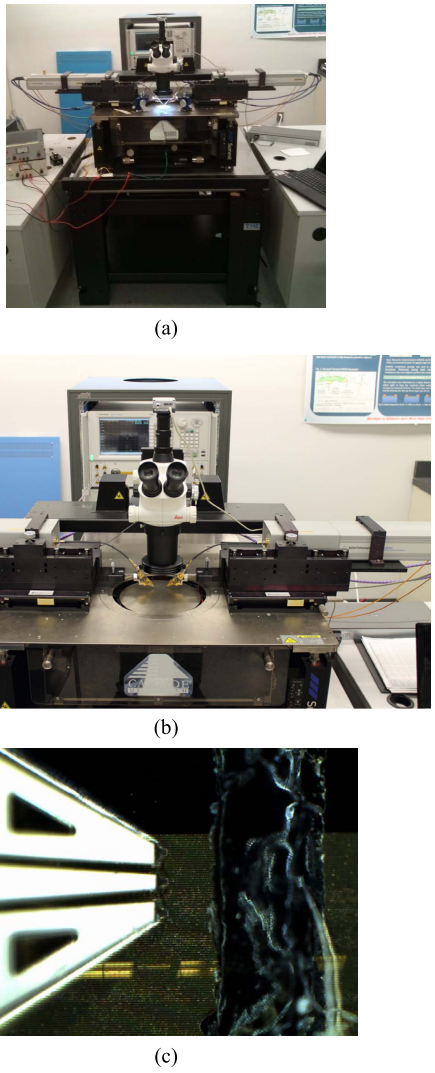

Fig. 12. (a) Cascade RF microprobe station with Agilent PNA. (b) Closer view of the station including a wafer mounting platform and RF probes. (c) RF probes on the left on IDE for measuring the film on the right.

since it contains the effect of the impedance of substrate and capping layer. Hence, Z_{GLAD} has to be extracted from device measurements (Z_{in}). The extraction requires knowing the equivalent impedance network of the whole device which is depicted in Fig. 15. This frequency-dependent model is developed based on the physical current paths inside the device and consists of generalized impedances that are recalculated at each measurement frequency. The input current first passes though the GLAD film before branching into two equal current paths through the capping layer and back through the GLAD film to ground.

From these measurements, the parasitic effects of the test traces and capping layer were extracted. After measuring the entire structure (Z_{in} in Fig. 15), the film and epoxy were manually removed by scraping with a dc probe. After removal of the film, the substrate was measured in the same probe location to determine the impedance of the substrate and gold test lines (Z_{sub}). The measured impedance of the substrate was subtracted from the device measurement using the circuit

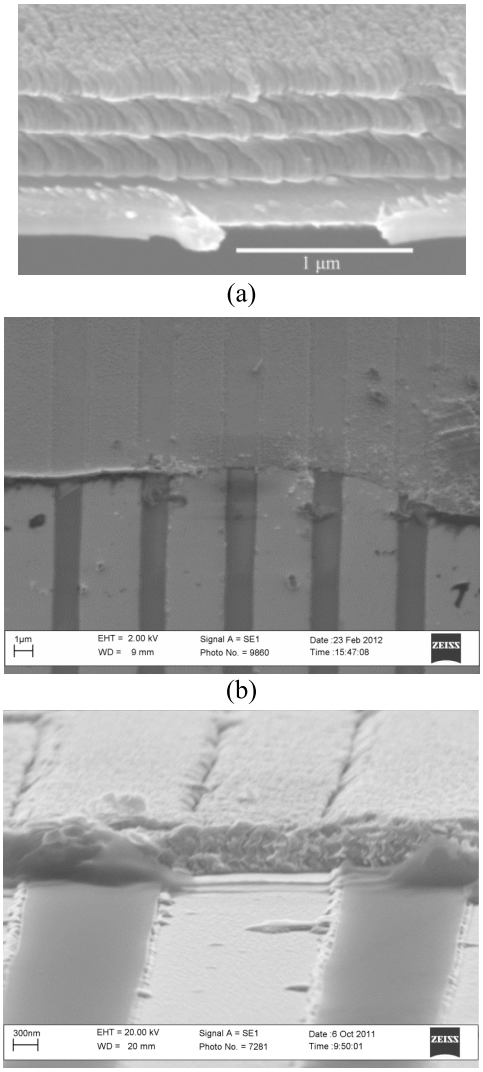

Fig. 13. (a) SEM image of film. (b) Top and (c) perspective views of film on IDE.

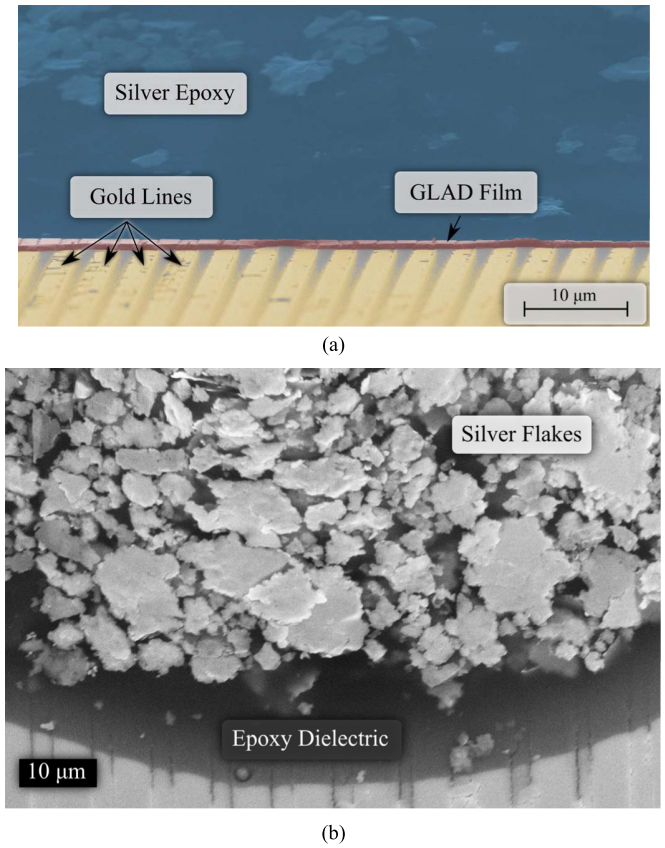

Fig. 14. (a) SEM image of the nanostructure of the film showing the entire film cross section on top of gold lines. (b) SEM picture of the silver flakes on top of the GLAD film. The epoxy used was high conductivity silver conductive epoxy from MG Chemicals (product number 8331-14G).

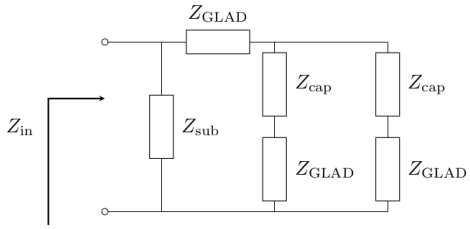

Fig. 15. Circuit model to extract the effect of the film.

model in Fig. 15. The effect of the epoxy was extracted by simulation in HFSS (the model is shown in Fig. 16).

The simulated impedance of the epoxy was used as Z_{cap} to fully extract the effect of the nanostructured film. The measured extracted inductance is depicted in Fig. 17. It is observed that the inductance is approximately constant over the 60 GHz of bandwidth as expected from simulations.

The measured results show 0.1 nH of inductance for a closed path from signal to ground. To find the field distribution inside the film, the equivalent homogeneous model is simulated as in Fig. 18(a). Fig. 18(b) shows the side view of the model showing the direction of current from signal to ground. Fig. 18(c) shows the magnetic ($\boldsymbol{H}$) field distribution on the model from top view. It is observed that the field penetrates into the film about 2 μm from the port, indicating that skin depth. The restricted field indicates that the portion of the material that contributes to the inductance is reduced from the physical area connected by the epoxy.

To find the inductance density, the effective area through which current passes should be found. According to the simulations, the current is constrained to a narrow film between signal and ground electrode with a size of about 0.4 μm $\times$ 35 μm. Considering the reduced area and the results in Fig. 17, the proposed structure results in 6.5 pH $\cdot$ μm^{-2} which is 60 times larger than the value reported in the literature for conventional 2-D microinductors.

The device's overall inductance can be tailored to the required design. For instance, for the values shown here at 40 GHz, the resulting reactance is 22.6 Ω. To achieve higher inductances, one can connect multiple transitions in series or simply increase the height of the inductors.

Fig. 19 shows the Q of the measured inductors which is calculated by dividing the extracted measured imaginary and real part of impedance. For the frequencies measured, the resistance was less than 18 Ω, including the contact resistance between the film and the gold–silver contacts. The quality factor linearly increases up to 70 GHz (reaching 3),

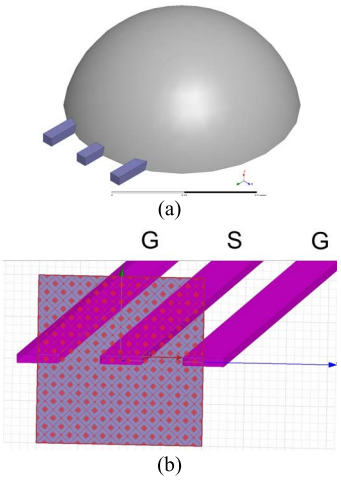

Fig. 16. (a) Simulation model of the silver epoxy. The blue lines on the left are the G–S–G probe lines which end on the surface of the silver epoxy (gray). (b) Waveport and the excitation vector used in ANSYS HFSS. Linewidth = 50 μm. Pitch = 100 μm.

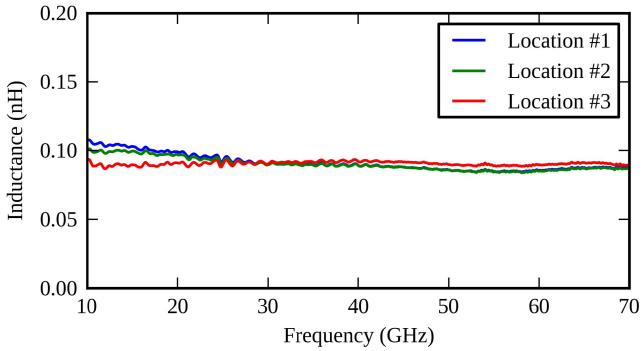

Fig. 17. Extracted inductance value for a single signal to ground return path.

indicating that the performance of these inductors may continue to improve above 70 GHz. Fig. 19 also shows the simulated Q of an effective anisotropic medium as in Fig. 9. The parametric values for Ni are chosen based on previously measured data reported in [27] with nanoscale conductivity of 75 000 S/m. The agreement of simulated and measured results verifies the anisotropic homogeneous model for GLAD film.

To synthesize a required inductance value (L) using GLAD film, the following steps should be taken. First, the helix and array sizes are found from SEM image of fabricated prototypes; the surface density of inductance (β) is calculated by simulating a 5×5 array with real sizes; the film area ($S = x \times y$) is calculated as $S = L/\beta$; knowing that x is equal to skin depth, y is calculated. Finally, the connecting electrode sizes are adjusted for y.

B. Power Handling

In practical RF devices, it is often necessary to use high-power signals. However, high powers are often associated with high currents that create strong magnetic fields. In strong magnetic fields, the effective permeability of high-permeability materials decreases due to magnetic saturation [29]. The inductance of the GLAD film was measured over a range of powers from -20 to $+10$ dBm to study how power affects the inductance of the film.

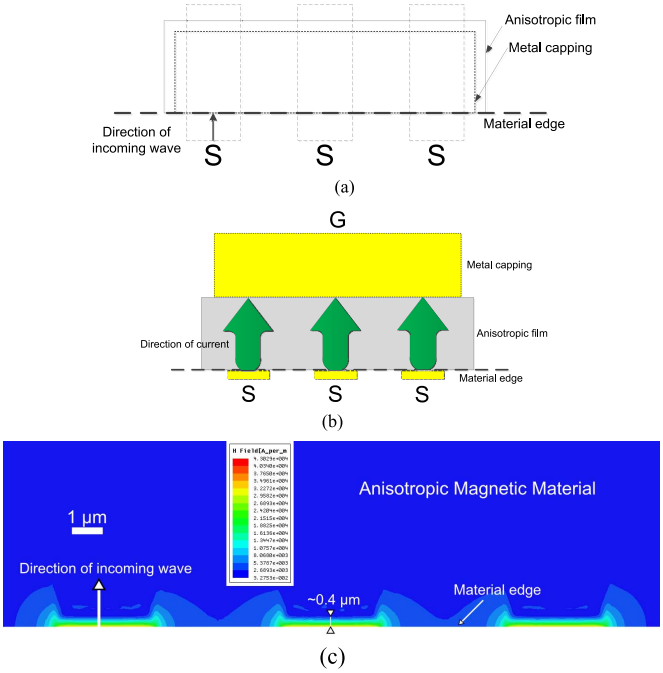

Fig. 18. Simulation model for inspecting the field distribution inside the nanowire film. (a) Top view—three IDEs as signal lines and a metal capping as ground electrode. (b) Side view—the direction of current through the film from S to G is shown by arrows. (c) Top view—the H-field distribution at 70 GHz at the edge of nanowire film.

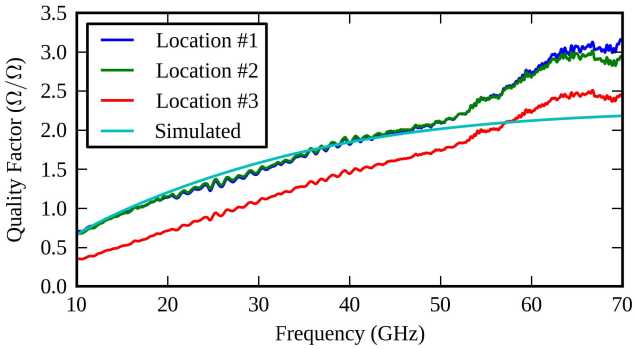

Fig. 19. Measured and simulated quality factor for the film. These locations are picked randomly to test the repeatability and reliability of the measurement method.

Fig. 20 shows the raw inductance measurement for the test device over a range of powers from -20 to 10 dBm. Two different devices were measured, and three measurement frequencies are shown. The results indicate that the measured inductance is approximately constant over the powers reported. Device #2 does show a slight reduction in inductance for 50 and 60 GHz, however, this reduction is small and still results in a very high inductance per area. Measurements at higher powers are required to demonstrate the expected reduction due to saturation in Ni.

V. Filling Material Enhancement

Since nanostructured thin films have voids in the material, it is possible to change the bulk material parameters, and therefore the inductance by filling this space with other materials. As shown for the single helix in Fig. 8, the inductive performance of the nanostructured helix film is strongly

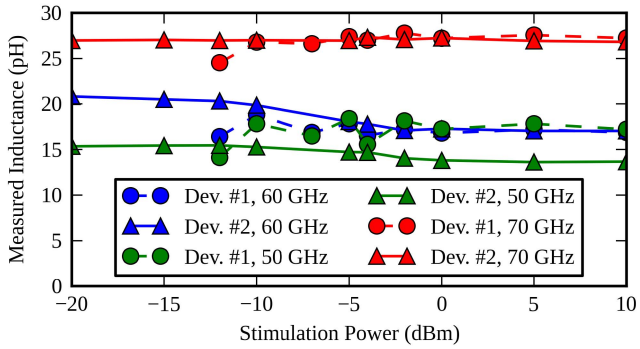

Fig. 20. Measured inductance by stimulation power. Two devices were measured at 50-, 60-, and 70-GHz frequencies and at input powers ranging from −20 to 10 dBm. Device #1 shows a constant trend, independent of stimulation power. Device #2 shows a slight decrease (for 50 and 60 GHz) in inductance as the power is increased, however, at 70 GHz, the inductance is constant across the range of powers measured.

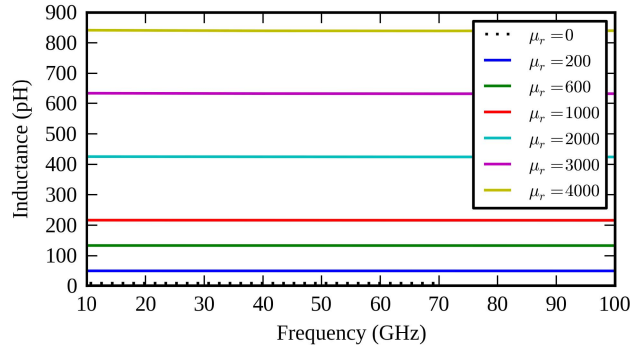

Fig. 21. Inductance of a 3 × 3 helix array in a homogenous, isotropic, and ideal magnetic material. The inductance is constant between 1 and 100 GHz and increases with the permeability of the material.

dependent on the permeability of the film. The permeability can be improved by adding a high permeability ferrite as a filling material.

To study the effect of increasing the permeability of the material, a 3 × 3 array of the helices was simulated with a penetrating material of various permeabilities. To determine solely the effect of the permeability enhancement, the simulated film had a conductivity of zero. Fig. 21 shows the helix's inductance as the permeability of the filling medium is increased. The resulting inductance is proportional to the surrounding material's permeability. Importantly, the inductance is increased by orders of magnitude with only a small increase in relative permeability over free space.

An increase in relative permeability to 600 results in over 0.133 nH for the helix array. The quality factor is shown in Fig. 22. Increases in the permeability of the filling material cause large gains in the quality factor.

The resulting quality factor for an effective medium of $\mu_r = 800$ is over 16 times larger than the quality factor for the free space material. Therefore, even small changes in the effective permeability of the film result in significant gains in quality factor.

Nonconductive high-permeability materials can be realized by solving magnetic (Ni) nanoparticles into photoresists [6]. To fill the GLAD film voids, this ferrite photoresist can be dispensed over the GLAD substrate and the substrate is spun at a high angular velocity, as a postdeposition treatment as it

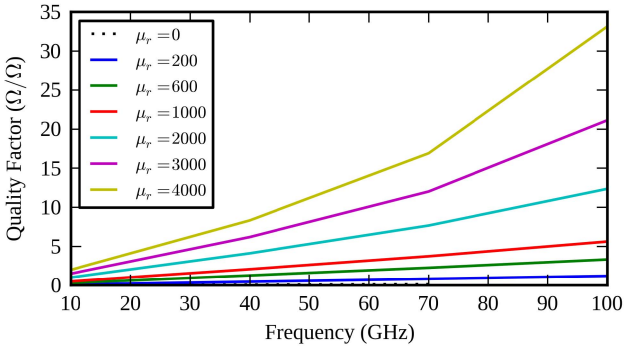

Fig. 22. Simulated quality factor of a 3 × 3 helix array in a material of varying permeability. The quality factor for the helix array embedded in a magnetic material increases with frequency and with magnetic permeability of the material.

has been done in [19]. In certain frequency regimes, nonconductive magnetic materials can exhibit high permeabilities and further research into nanoscale materials may produce high-permeability materials in the millimeter-wave regime.

VI. Conclusion

This paper has introduced an area-efficient implementation of on-chip inductors using nanoscale structures deposited by GLAD. The nanostructured helices produce an effective medium with anisotropic conductivity. These structures were simulated by Ansys HFSS and were predicted to have extremely high inductance densities compared with traditional planar inductors. The simulated structures were fabricated out of Ni and were measured to have an inductance of 0.1 nH with an inductance density of 6 pH · μm^{-2}. The inductance values were fairly constant between 10 and 70 GHz. The inductance density is considerably higher than previously reported densities for practical planar inductors. The proposed vertical nanostructures were fabricated using a single-step PVD process that is compatible with CMOS technology, allowing for direct integration of this process with existing CMOS devices. The proposed structure could potentially lead to ultraminiaturized wideband inductors reducing the die area and cost of RF and millimeter-wave ICs.

Acknowledgment

The authors would like to thank Prof. M. Brett and Dr. M. Taschuk for sample preparation and constructive discussions. The authors would also like to thank M. Summers and J. Sorge for Fig. 1.

References

[1] X. H. Lai, F. Ding, Z. G. Xu, W. G. Wu, J. Xu, and Y. L. Hao, "Suspended nanoscale solenoid metal inductor with tens-nH level inductance," in *Proc. IEEE 21st Int. Conf. Micro Electro Mech. Syst. (MEMS)*, Jan. 2008, pp. 1000–1003.

[2] T. H. Lee, *The Design of CMOS Radio-Frequency Integrated Circuits*, 1st ed. Cambridge, U.K.: Cambridge Univ. Press, 1998.

[3] T. O. Dickson, M.-A. LaCroix, S. Boret, D. Gloria, R. Beerkens, and S. P. Voinigescu, "30–100-GHz inductors and transformers for millimeter-wave (Bi)CMOS integrated circuits," *IEEE Trans. Microw. Theory Techn.*, vol. 53, no. 1, pp. 123–133, Jan. 2005.

[4] H.-Y. Tsui and J. Lau, "An on-chip vertical solenoid inductor design for multigigahertz CMOS RFIC," *IEEE Trans. Microw. Theory Techn.*, vol. 53, no. 6, pp. 1883–1890, Jun. 2005.
[5] J. Zou, C. Liu, D. R. Trainor, J. Chen, J. E. Schutt-Aine, and P. L. Chapman, "Development of three-dimensional inductors using plastic deformation magnetic assembly (PDMA)," *IEEE Trans. Microw. Theory Techn.*, vol. 51, no. 4, pp. 1067–1075, Apr. 2003.
[6] K. Tsubaki, Y. Nakajima, T. Hanajiri, and H. Yamaguchi, "Proposal of carbon nanotube inductors," *J. Phys., Conf. Ser.*, vol. 38, pp. 49–52, May 2006.
[7] O. F. Mousa, B. C. Kim, J. Flicker, and J. Ready, "A novel design of CNT-based embedded inductors," in *Proc. 59th Electron. Compon. Technol. Conf. (ECTC)*, 2009, pp. 497–501.
[8] G. Stojanovic, T. Ljikar, and R. Sordan, "Scaling meander inductors from micro to nano," in *Proc. Int. Semicond. Conf.*, vol. 1. 2006, pp. 93–96.
[9] R. Yang, H. Qian, J. Li, Q. Xu, C. Hai, and Z. Han, "SOI technology for radio-frequency integrated-circuit applications," *IEEE Trans. Electron Devices*, vol. 53, no. 6, pp. 1310–1316, Jun. 2006.
[10] I. A. Ukaegbu, K.-S. Choi, O. Hidayov, J. Sangirov, T.-W. Lee, and H.-H. Park, "Small-area and high-inductance semi-stacked spiral inductor with high Q factor," *IET Microw. Antennas Propag.*, vol. 6, no. 8, pp. 880–883, 2012.
[11] J. M. López-Villegas, J. Samitier, C. Cané, P. Losantos, and J. Bausells, "Improvement of the quality factor of RF integrated inductors by layout optimization," *IEEE Trans. Microw. Theory Techn.*, vol. 48, no. 1, pp. 76–83, Jan. 2000.
[12] C. H. Ahn and M. G. Allen, "Micromachined planar inductors on silicon wafers for MEMS applications," *IEEE Trans. Ind. Electron.*, vol. 45, no. 6, pp. 866–876, Dec. 1998.
[13] F. Gianesello *et al.*, "Integration of ultra wide band high pass filter using high performance inductors in advanced high resistivity SOI CMOS technology," in *Topical Meeting Silicon Monolithic Integr. Circuits RF Syst., Dig. Papers*, Jan. 2006, p. 4.
[14] Y.-H. Cho, S.-C. Hong, and Y.-S. Kwon, "A novel active inductor and its application to inductance-controlled oscillator," *IEEE Trans. Microw. Theory Techn.*, vol. 45, no. 8, pp. 1208–1213, Aug. 1997.
[15] K. Kamata, S. Suzuki, M. Ohtsuka, M. Nakagawa, T. Iyoda, and A. Yamada, "Fabrication of left-handed metal microcoil from spiral vessel of vascular plant," *Adv. Mater.*, vol. 23, no. 46, pp. 5509–5513, 2011.
[16] H. Li, C. Xu, N. Srivastava, and K. Banerjee, "Carbon nanomaterials for next-generation interconnects and passives: Physics, status, and prospects," *IEEE Trans. Electron Devices*, vol. 56, no. 9, pp. 1799–1821, Sep. 2009.
[17] C. Yang *et al.*, "On-chip soft-ferrite-integrated inductors for RF IC," in *Proc. Int. Solid-State Sens., Actuators Microsyst. Conf. (TRANSDUCERS)*, 2009, pp. 785–788.
[18] A. Seilis, M. Daneshmand, K. Moez, M. Taschuk, and M. Brett, "Vertically-aligned nano-scale integrated inductors," in *Proc. IEEE MTT-S Int. Microw. Symp.*, Jun. 2013, pp. 1–3.
[19] M. T. Taschuk, M. M. Hawkeye, and M. J. Brett, "Glancing angle deposition," in *Handbook of Deposition Technologies for Films and Coatings*, P. M. Martin, Ed., 3rd ed. Boston, MA, USA: William Andrew Pub., 2010, pp. 621–678.
[20] A. G. Seilis, "Nanostructured inductors for millimetre-wave applications," M.S. thesis, Dept. Elect. Comput. Eng., Univ. Alberta, Edmonton, AB, Canada, 2013.
[21] M. R. Kupsta, M. T. Taschuk, M. J. Brett, and J. C. Sit, "Overcoming cap layer cracking for glancing-angle deposited films," *Thin Solid Films*, vol. 519, no. 6, pp. 1923–1929, 2011.
[22] J. J. Steele, G. A. Fitzpatrick, and M. J. Brett, "Capacitive humidity sensors with high sensitivity and subsecond response times," *IEEE Sensors J.*, vol. 7, no. 6, pp. 955–956, Jun. 2007.
[23] J. Zhang, N. Xi, H. Chen, and K. W. C. Lai, "Fabrication and experimental testing of individual multi-walled carbon nanotube (CNT) based infrared sensors," in *Proc. IEEE Sensors*, Oct. 2007, pp. 511–514.
[24] D. J. Griffiths, *Introduction to Electrodynamics*, 3rd ed. Upper Saddle River, NJ, USA: Prentice-Hall, 1999.
[25] K. Okamoto and K. Itoh, "Incidence angle dependences of columnar grain structure and texture in obliquely deposited iron films," *Jpn. J. Appl. Phys.*, vol. 44, no. 3, pp. 1382–1388, Mar. 2005.
[26] Y. Zhuang, M. Vroubel, B. Rejaei, and J. N. Burghartz, "Thin film magnetic materials for RFIC passives," in *Proc. Bipolar/BiCMOS Circuits Technol. Meeting*, 2005, pp. 26–32.
[27] M. M. Hawkeye, M. T. Taschuk, and M. J. Brett, *Glancing Angle Deposition of Thin Films: Engineering the Nanoscale*. New York, NY, USA: Wiley, 2014.
[28] J. M. LaForge, G. L. Ingram, M. T. Taschuk, and M. J. Brett, "Flux engineering to control in-plane crystal and morphological orientation," *Crystal Growth Design*, vol. 12, no. 7, pp. 3661–3667, Jul. 2012.
[29] F. Brailsford, *Magnetic Materials*. London, U.K.: Methuen, 1960.

Aaron Seilis, photograph and biography not available at the time of publication.

Hamid Moghadas, photograph and biography not available at the time of publication.

Kambiz Moez, photograph and biography not available at the time of publication.

Mojgan Daneshmand, photograph and biography not available at the time of publication.